Charge-current paper

xFitter Developers' team:

[1]Address(es) of author(s) should be given

Abstract

1 Introduction

The Deep-inelastic-scattering (DIS) experiments tradition-ally were an important probe of pQCD and used to pre-cise determination of parton distribution functions (PDFs) at lepton-nucleon and nucleon-nucleon colliders. The vari-ous dedicated experiments such as HERA have been per-formed by colliding electron and positron with proton to in-vestigate the nucleon structure. The broad kinematic region of charge-current (CC) and Neutral-current (NC) DIS data at HERA base on negative transverse momentum squared Q^2 and Bjorken variable x caused that these data play import-ant role on modern determination of the parton distribution function [1–3].

In the standard model, the charm quark has an important role in the investigation of the nucleon structure [4–6]. The pQCD calculation assumed that charm charm distribution is generated perturbatively by gluon and light quark splitting functions and it's mass depended strongly on the DIS coef-ficient functions which is are known up to second order in the strong coupling constant in the NC process considering heavy quark mass effects[7, 8] . The heavy quark mass ef-fects in the CC process, calculated up to $\mathcal{O}(\alpha_s^2)$ in Refs. [9–12] and recently completed in Ref. [13] which is available up to $\mathcal{O}(\alpha_s^2)$ at large Q^2 for the xF_3 structure function [14].

Although the heavy quarks specially charm quark, have an important role in many process even beyond the standard model, there are some process which is provides direct ac-cess to the strange sea quark, one of the significant part of the nucleon structure and the completed and accurate know-ledge on this topic help us to the better understanding of the

properties of the sea quark and also the nucleon structure in the process with a strange quark mediated by weak charge boson in association with charm jet [15, 16] and also neut-rino and anti-neutrino production measured by CCFR [17], NuTev [18], CHORUS [19], CDHSW [20] and NOMAD [21] collaborations that give useful information but limited on the normalisation and shape of the $s(x) + \bar{s}(x)$. for the first time HERMES collaboration extracted the $s(x) + \bar{s}(x)$ from charged lepton DIS data and complementary to the neutrino results [22].

On the other hand the charm production mediated by electroweak gauge boson at hadron colliders provide import-ant information on strange and charm quark distribution and complementary the DIS final state charm quark experiment [16]. Although CDF and D0 at Tevatron [23, 24] measured the charm quark cross section in association with W boson but these measurement is limited to 30% by low statist-ics. Some of the global QCD analyses in absence of sig-nificant experiential constraints, at some low factorisation scale, extracted the strange $s(x)$ and anti-strange $\bar{s}(x)$ given by $s(x) = \bar{s}(x) = r_s[\bar{u} + \bar{d}]/2$ [25, 26] here r_s is the fraction of the strange quark density in the proton that reported value by ATLAS at the scale $Q - 0 = 1.9$ GeV^2 and $x = 0.023$ is 1.19 [27]. The LHC tried to provide a more precise meas-urement and CMS and ATLAS collaboration performed ... By eliminated the isoscalar between strange and anti-strange distribution, the CTEQ [16] and MSTW [28] extracted the strange and anti-strange distribution at NLO. This paper or-ganized as follow, in the Sec. ....

2 Theoretical predictions for charm CC production at LHeC

Theoretical predictions are calculated for electroweak charm CC production in ep collisions at the LHeC at centre-of-

mass energy $\sqrt{s} = 1.3$ TeV, using a variety of heavy flavour schemss. The predictions are provided for unpolarised beams in the kinematic range $100 < Q^2 < 100000$ GeV^2 $0.0001 < x_{Bj} < 0.25$. They are calculated as reduced cross sections at different Q^2, x_{Bj} and y points.

Experimentally, however, not charm quarks but charmed hadrons (or rather their decay products) are registered in the detectors. Therefore, extrapolation to the inclusive charm production cross section has to be carried out in a model dependent way. Furthermore, in CC charm quarks in the final state can be produced via both electroweak and QCD production processes. The former leads to an odd number of charm quarks in the final state with the W boson having the same electric charge as the sum electric charges of final state charm quarks, while the latter creates an even number of charm quarks with total electric charge equal to zero. If the electric charge of the tagged charm quark can be accessed experimentally (e.g. when reconstructing D mesons) the QCD contribution can be excluded by taking the difference of the yields in the events with odd and even numbers of charm quarks, otherwise the QCD contribution can be subtracted only in a model dependent way.

The charm CC process directly depends on the CKM matrix. Here, the CKM matrix elements V_{cd} and V_{cs} are of particular interest. The values used are $V_{cd} = 0.2252$ and $V_{cs} = 0.9734$. Three different heavy-flavour schemes are employed, all including a full treatment of charm mass effects up to NLO[1], i.e. $O(\alpha_s)$, and described here for the particular application to charged current electron-proton reactions. The standard fixed flavour number scheme (FFNS A) uses three light flavours in both PDFs and α_s evolution, while heavy flavours (here: charm) are produced exclusively in the matrix element part of the calculation. This scheme has been used e.g. for the PDF determinations and cross-section predictions of the ABM(P) group [29, 30], as well as in the FF3A variant of HERAPDF [2], and implemented in xFitter through the OPENQCDRAD package [31]. The "B" variant of the fixed-order-next-to-leading-log scheme (FONLL B) combines the NLO ($O\alpha_s$) massive matrix elements of the fixed flavour scheme with the NLO ($O\alpha_s$) massless treatment of the zero-mass variable flavour number scheme (ZM-VFNS), allowing the number of active flavours (3, 4, or 5) to vary with scale, and all-order next-to-leading log resummation of (massless) terms beyond NLO. It thus explicitly includes charm and beauty both in the PDFs and in the evolution of the strong coupling constant. Whenever terms would be double-counted in the merger of the two schemes the massless terms are eliminated in favour of retaining the massive terms. The FONLL is heavily used by the NNPDF group [Ball:2017nwa] and implemented in xFitter through the APFEL package [32]. Finally a variant of the fixed fla-

---

[1]The $O(\alpha_s^2)$ corrections quoted earlier are not yet avaialble in the context of the xFitter setup.

vour number scheme known as the 'mixed' scheme or FFNS B [4] is used. In this scheme, the number of active flavours is still fixed (here: to 3) in the PDFs, relying exclusively on $O(\alpha_s)$ fully massive matrix elements for charm production, while the number of flavours is allowed to vary in the virtual corrections of the alphas evolution. Corrections to this evolution involving heavy flavour loops are thus included and resummed to all orders, as in the VFNS schemes, while no resummation is applied to other higher order corrections. This procedure will catch a large fraction of the "large logs" which might spoil the fixed-flavour scheme convergence at very high scales, and is possible since the masses of the charm and beauty quarks provide natural cutoffs for infrared and collinear divergences. This scheme was used in the HERAPDF FF3B variant [2] and in applications of the HVQDIS program [4]. In general the transition from the FFNS A to the FFNS B scheme requires a readjustment of the treatment of matrix elements involving heavy flavour loops, but in the specific case of charged current no such loops occur up to NLO (at NNLO they will), such that the same matrix elements can be used for both schemes, and here the only difference is the alphas evolution.

In summary, the schemes used are

- FFNS A with $n_f = 3$ at NLO and ABMP16 [30] or HERAPDF2.0 FF3A [2] NLO PDF set,
- FFNS B with $n_f = 3$ at NLO and ABMP16 [30] or HERAPDF2.0 FF3B [2] NLO PDF set,
- FONLL-B with $n_f = 3$ and NNPDF3.1 NLO PDF set [33].

All calculations are interfaced in xFITTER and available in the scheme using the running $\overline{MS}$ charm mass, $m_c(m_c)$. The $\overline{MS}$ charm mass is set to $m_c(m_c) = 1.27$ GeV [34], and α_s is set to the value used for the corresponding PDF extraction ($\alpha_s(M_Z) = 0.1191$ for ABMP16, and $\alpha_s(M_Z) = 0.118$ for NNPDF3.1). The renormalisation and factorisation scales are chosen to be $\mu_r = \mu_f = Q^2$.

To estimate theoretical uncertainties, the two scales are simultaneously varied up and down by factor 2. In the case of the FONLL-B calculations, also the independent μ_r and μ_f variations are checked. Furthermore, the PDF uncertainties are propagated to the calculated theoretical predictions, while the uncertainties arising from varying the charm mass $m_c(m_c) = 1.27 \pm 0.03$ GeV are smaller than 1% and therefore neglected. In the FONLL-B scheme, as a cross check, the calculation was performed with the pole charm mass $m_c^{pole} = 1.51$ GeV which is consistent with the conditions of the NNPDF3.1 extraction [33]. The obtained theoretical predictions differ from the ones calculated with $m_c(m_c) = 1.27$ GeV by less than 1%. The total theoretical uncertainties are obtained by adding in quadrature the scale and PDF uncertainties.
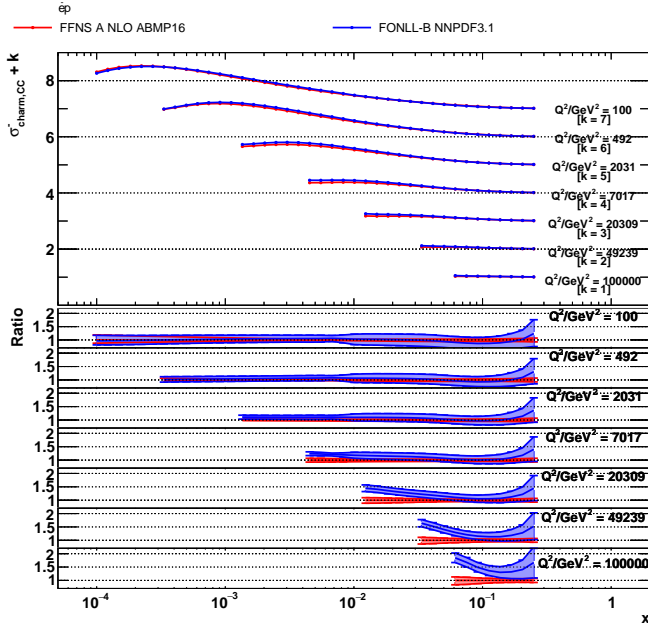
Figure 1 The theoretical predictions with their total uncertainties for charm CC production at the LHeC as a function of x_{Bj} for different values of Q^2 calculated in the FFNS A and FONLL-B schemes. The bottom panel display the theoretical predictions normalised to the nominal values of the FFNS A predictions.
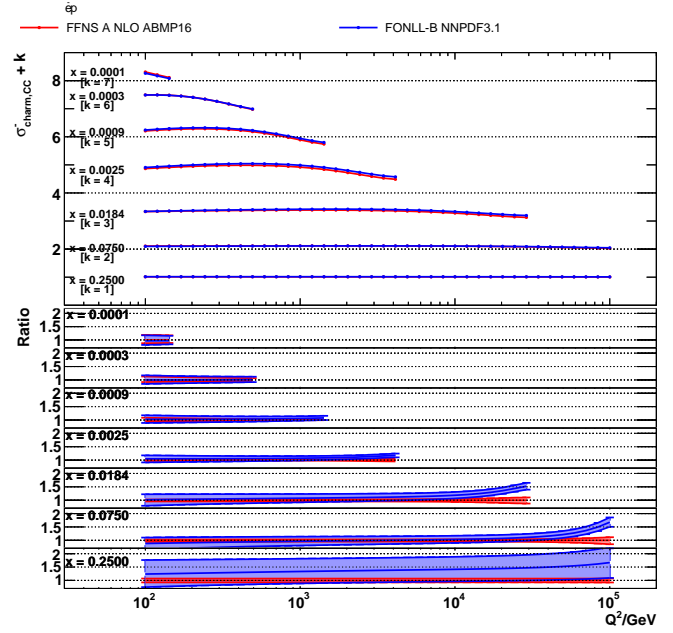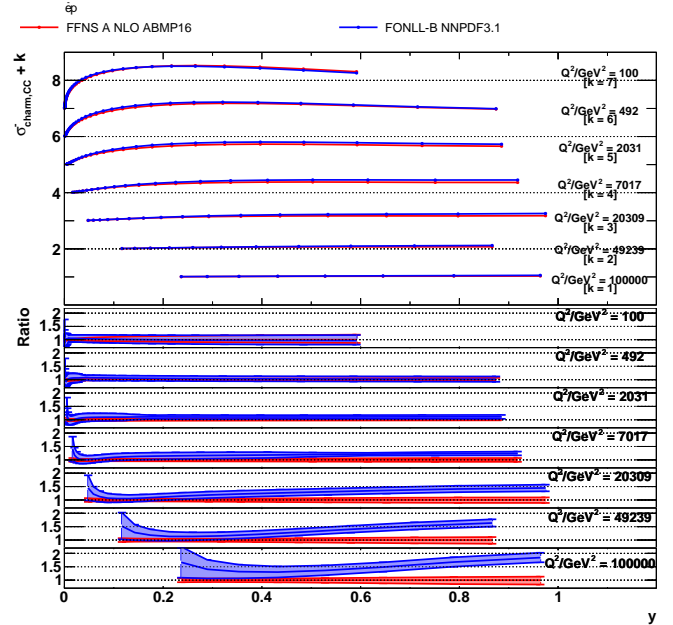

Figure 2 The theoretical predictions with their total uncertainties for charm CC production at the LHeC as a function of Q^2 for different values of x_{Bj} calculated in the FFNS A and FONLL-B schemes. The bottom panel display the theoretical predictions normalised to the nominal values of the FFNS A predictions.

## 2.1 Comparison of theoretical predictions in the FFNS A and FONLL-B schemes

Figures 1, 2 and 3 show theoretical predictions with their total uncertainties in both schemes as a function of x_{Bj} for different values of Q^2, as a function of Q^2 for different values of x_{Bj}, and as a function of y for different values of Q^2, respectively. The FFNS A and FONLL-B agree reasonably well, within uncertainties of moderate size, in the bulk of the phase space. However, in phase space corners such as high $Q^2 \gtrsim 10000\,\mathrm{GeV}^2$ or low $y \lesssim 0.05$ the predictions in the two schemes differ by more than 50%, and these differences are not covered by the theoretical uncertainties.

In Fig. 4 the PDF and scale uncertainties of charm CC cross sections as a function of Q^2 for different values of x_{Bj} calculated in the FFNS A and FONLL-B schemes are shown. On average, in the FONLL-B scheme both the PDF and scale uncertainties exceed those in the FFNS A scheme. Furthermore, Fig. 5 shows the impact of separate scale variations in the two schemes. In the FONLL-B scheme, the variation of μ_f has a much larger impact on the predictions than the variation of μ_r, and thus it is dominant for the resulting scale uncertainties. **[Valerio, could you please discuss more here?]** Only the simultaneous $\mu_f = \mu_r$ variation is available in the implementation of the FFNS A scheme.

To explore whether the differences between the two sets of theoretical predictions appear due to the different treatment of heavy quarks or due to different PDF sets, theoret-

Figure 3 The theoretical predictions with their total uncertainties for charm CC production at the LHeC as a function of y for different values of Q^2 calculated in the FFNS A and FONLL-B schemes. The bottom panel display the theoretical predictions normalised to the nominal values of the FFNS A predictions.
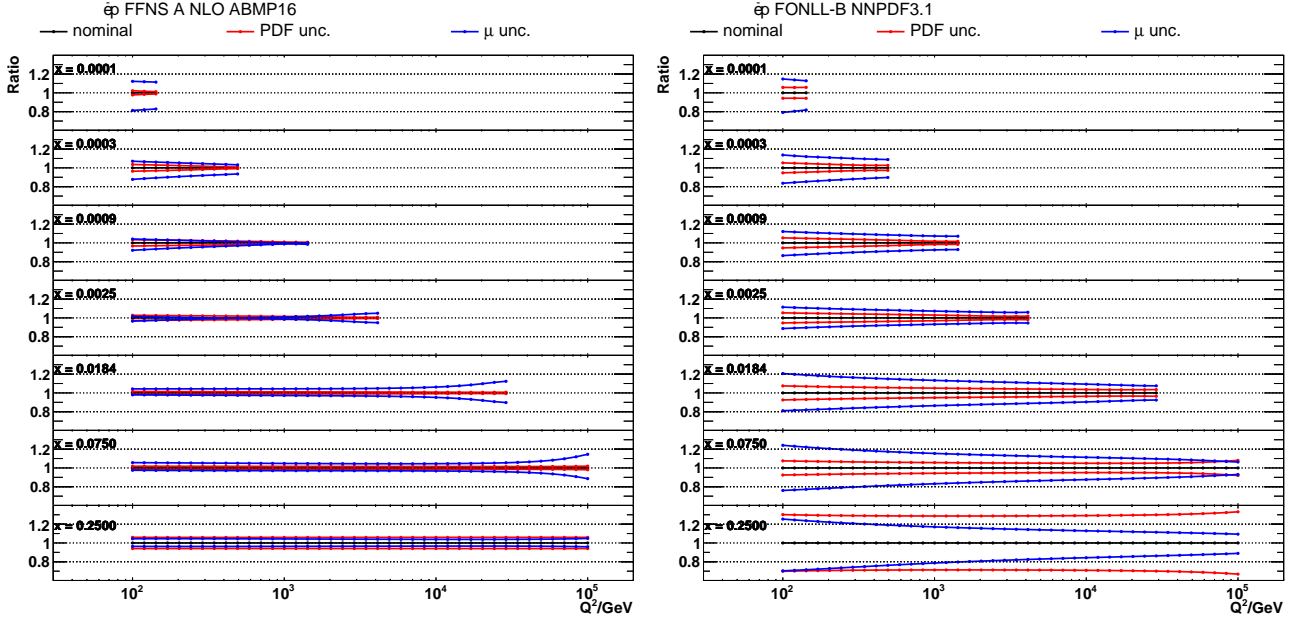
Figure 4 Relative theoretical uncertainties of charm CC predictions for the LHeC as a function of Q^2 for different values of x_{Bj} calculated in the FFNS A and FONLL-B schemes. The PDF and scale uncertainties are shown separately.
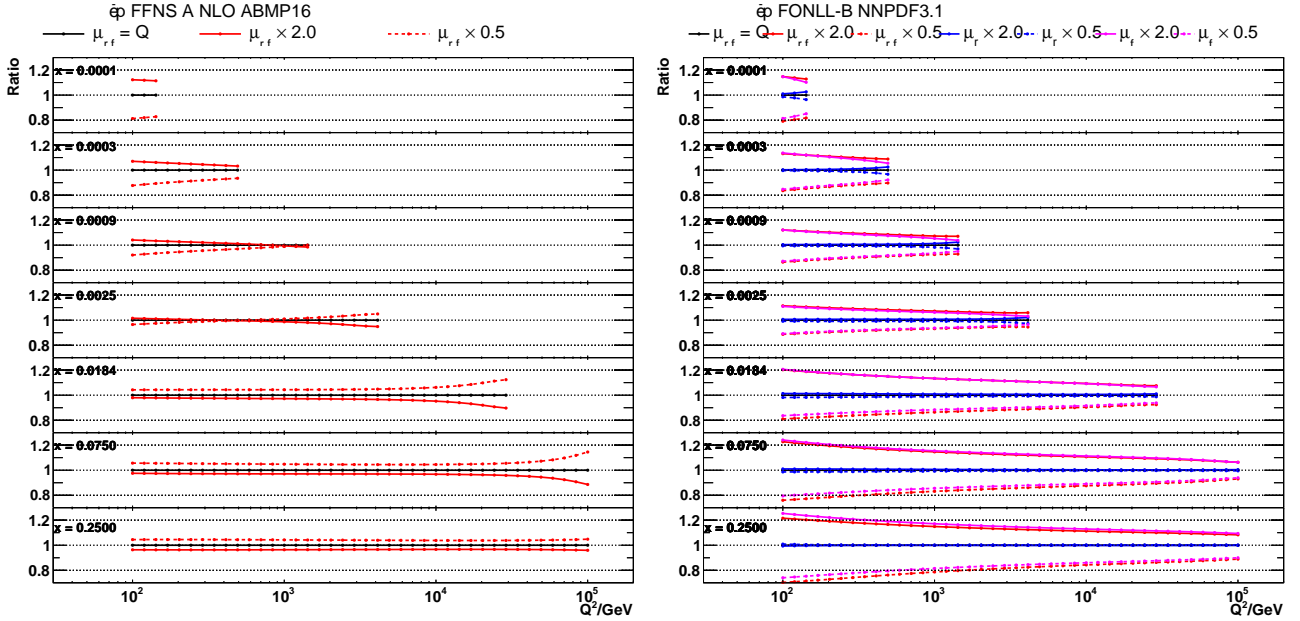
Figure 5 The impact of separate scale variations on charm CC predictions for the LHeC as a function of Q^2 for different values of x_{Bj} calculated in the FFNS A and FONLL-B schemes.

ical calculations in the FFNS A and FONLL-B schemes are repeated with PDF sets extracted from the fit to the HERA DIS data [2]. The fit settings follow the HERAPDF2.0 analysis [2]. In this study, consistent conditions of the PDF extraction eliminate possible differences between the predictions for the LHeC arising from the dissimilarities of the ABMP16 and NNPDF3.1 analysis. The obtained results are displayed in Figs. **??**–**??**. The differences between the FFNS A and FONLL-B schemes in these predictions are similar to the ones displayed in Figs. 1–3 and prove that these differences arise due to the different treatment of heavy quarks in the two schemes.

Furthermore, the predictions in the FFNS A and FFNS B schemes calculated using the HERAPDF2.0 FF3A and HERAPDF2.0 FF3B PDF sets are displayed in Figs. **??**–**??**. Because of the similarities of the two HERAPDF2.0 PDF sets, the differences between the two sets of the predictions arise mainly due to the different treatment of heavy quarks

in the two schemes. Remarkably, the differences between FFNS A and FONLL-B predictions are similar to the ones between FFNS A and FFNS B, i.e. a larger part of these differences arise due to the different treatment of heavy quarks in $\alpha_s(\mu)$ running.

To explore whether the differences between the two sets of theoretical predictions appear due to the different treatment of heavy quarks or due to different PDF sets, theoretical calculations in the FFNS A and FONLL-B schemes are repeated with the HERAPDF2.0 sets extracted from the same HERA DIS data using coherent settings [2]. Furthermore, the predictions in the FFNS B scheme are produced using the HERAPDF2.0 FF3B PDF set and the FFNS A matrix elements, which are equaivalent to the FFNS B matrix elemenets at NLO for charm CC production. The obtained results are displayed in Fig. 6. The differences between the FFNS A and FONLL-B schemes in these predictions are similar to the ones displayed in Figs. 1–3 and prove that these differences arise due to the different treatment of heavy quarks in the two schemes. The FFNS B predictions are between the FFNS A and FONLL-B predictions, indicating that a large part of these differences arise due to the different treatment of heavy quarks in $\alpha_s(\mu)$ running.

Furthermore, to investigate the impact of the NNLO corrections available at $Q \gg m_c$ for the FFNS calculation, approximate NNLO predictions are obtained using the ABMP16 NNLO PDF set [29]. The results for the cross sections as a function of Q^2 for difference values of x_{Bj} are shown in Fig. 7, where they are compared to the NLO FFNS predictions from Fig. 2. The NNLO corrections do not exceed 10% and thus do not cover the differences between the FFNS A and FONLL-B theoretical predictions. Similar results are observed for cross sections as functions of other kinematic variables.

To better understand the differences between the FFNS and VFNS calculations, Fig.2*** which displays the cross section vs. Q^2 is particularly instructive. We see at low scales the FFNS and VFNS results coincide. When the μ scale is below the charm threshold scale (typically taken to be $\sim m_c$) the charm PDF vanishes and the FFNS and VFNS reduce to the same result.[2] For increasing scales, the VFNS resums the $\alpha_S \ln(\mu^2/m_c^2)$ contributions via the DGLAP evolution equations and the FFNS and VFNS will slowly diverge logarithmically. This behavior is observed in Fig.2*** and consistent with the characteristics demonstrated in Ref. [36].

More precisely, Ref. [36] used a matched set of $N_F = 3$ and $N_F = 5$ PDFs to study the impact of the scheme choice at large scales. They found the resummed contributions in the VFNS yielded a larger cross section than the FFNS (the

specific magnitude was x-dependent), and that for Q scales more than a few times the quark mass, the differences due to scheme choice exceeded the differences due to (estimated) higher order contributions [36].

2.2 Contributions from different partonic subprocesses

[perhaps this text would be more appropriate in an earlier theory section] The reduced charm CC production cross sections can be expressed as a linear combinations of the structure functions:

$$\sigma_{\text{charm,CC}}^{\pm} = 0.5(Y_+ F_2^{\pm} \mp Y_- x F_3^{\pm} - y^2 F_L^{\pm}),$$
$$Y_{\pm} = 1 \pm (1-y)^2. \tag{1}$$

In the simplified Quark Parton Model, where gluons are not present, the structure functions become:

$$F_2^+ = xD + x\overline{U},$$
$$F_2^- = xU + x\overline{D},$$
$$F_L = 0, \tag{2}$$
$$xF_3^+ = xD - x\overline{U},$$
$$xF_3^- = xU - x\overline{D}.$$

The terms xU, xD, $x\overline{U}$ and $x\overline{D}$ denote the sums of parton distributions for up-type and down-type quarks and antiquarks, respectively. Below the b-quark mass threshold, these sums are related to the quark distributions as follows:

$$xU = xu + xc,$$
$$x\overline{U} = x\overline{u} + x\overline{c},$$
$$xD = xd + xs, \tag{3}$$
$$x\overline{D} = x\overline{d} + x\overline{s}.$$

In the FFNS the charm quark density is zero. In the phase space corners $y \to 0$ and $y \to 1$, the following asymptotics take place:

$$y \to 0 : \sigma_{\text{charm,CC}}^{\pm} = F_2^{\pm} = xD(x\overline{D}) + xU(x\overline{U}),$$
$$y \to 1 : \sigma_{\text{charm,CC}}^{\pm} = 0.5(F_2^{\pm} \mp xF_3^{\pm}) = xU(x\overline{U}). \tag{4}$$

Thus the contribution from the strange quark PDF is suppressed at high y.

Figures 8, 9 and 10 show contributions from different partonic subprocesses for charm CC production cross sections in the FFNS A and FONLL-B schemes as a function of x_{Bj} for different values of Q^2, as a function of Q^2 for different values of x_{Bj}, and as a function of y for different values of Q^2, respectively. In both scheme, the strange quark PDF contributes only about 50% to total charm CC production. In particular, at high y its contribution drops to zero in favor of the gluon or charm quark PDF (see Fig. 10 and Eq. 4). Similar phenomena (although less pronounced) is observed

---

[2]Note that while the charm threshold scale μ_c is commonly set to the charm quark mass m_c, the choice of μ_c is arbitrary and amounts to a renormalzation scheme choice [35].
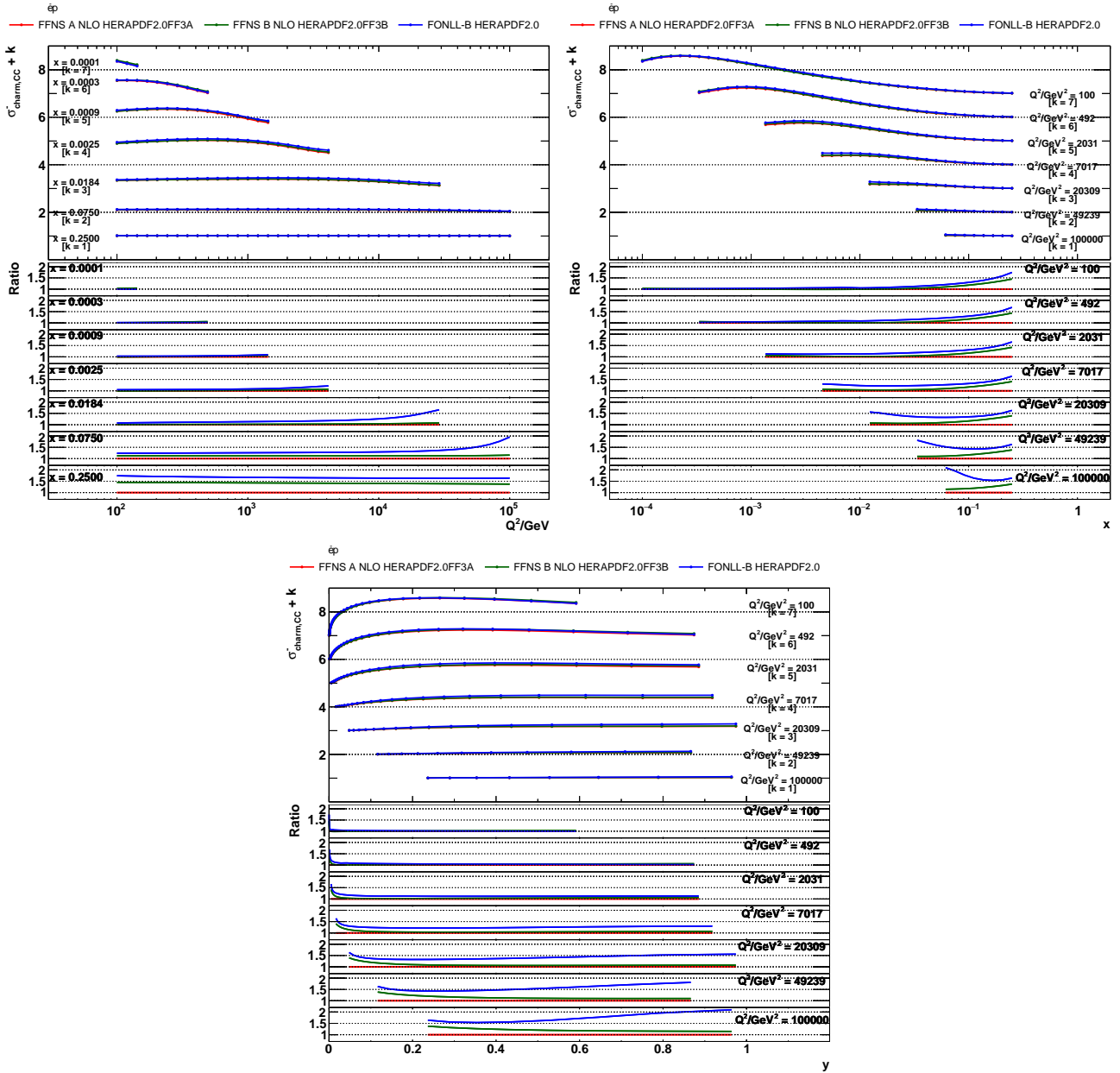
Figure 6 The theoretical predictions for charm CC production at the LHeC as a function of Q^2 (x_{Bj}, y) for different values of x_{Bj} (x_{Bj}, Q^2) obtained using the HERAPDF2.0 PDF sets in the FFNS A, FFNS B and FONLL-B schemes. The bottom panel display the theoretical predictions normalised to the nominal values of the FFNS A predictions.

at low x_{Bj} and/or high Q^2. In these phase space regions, the dominant contributions to the cross sections are the gluon PDF (in the FFNS) or the charm quark PDF (in the VFNS). Remarkably, these contributions as functions of Q^2, x_{Bj} and y behave qualitatively very similar in the FFNS and VFNS.

Figures 7,8,9*** display a particularly interesting pattern; the gluon contribution for the FFNS is strikingly similar to the charm contribution in the VFNS.

In the FFNS, the charm is produced predominantly from the explicit process $g\gamma \to c\bar{c}$. In contrast, for the VFNS the $g \to c\bar{c}$ splitting is implicit (internal to the proton and evolved with the DGLAP evolution equations); the charm parton then emerges from the proton to participate in the $c\gamma \to c$ process. The fundamental underlying process is the same in both the FFNS and VFNS, but the factorization boundary between the PDF and the hard scattering cross section, $f \otimes \hat{\sigma}$, (determined by μ and the scheme choice) is different.[3]

---

[3]Note there is a "subtraction" term ($g \to c\bar{c} \otimes c\gamma \to c$) which closely matches the LO $c\gamma \to c$ process, but this $\mathcal{O}(\alpha\alpha_S)$ process is contained in the NLO gluon-initiated contribution.
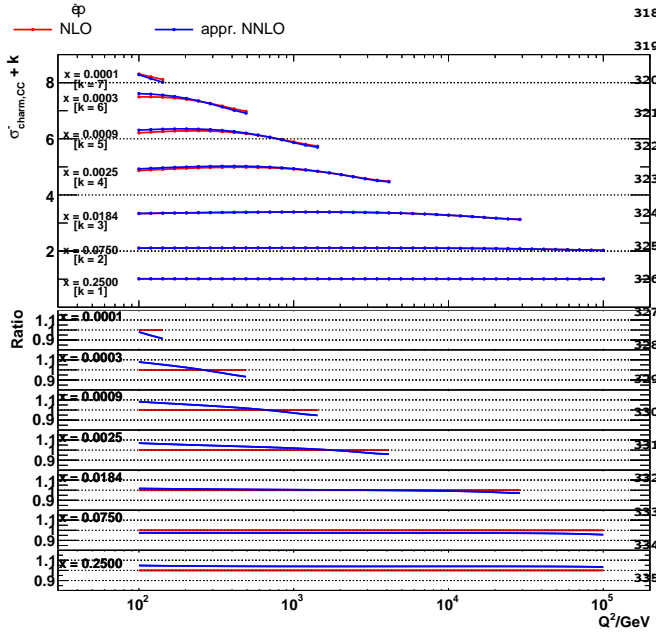
Figure 7 The theoretical predictions with their total uncertainties for charm CC production at the LHeC as a function of Q^2 for different values of x_{Bj} calculated in the FFNS A scheme at NLO and approximate NNLO. The bottom panel display the theoretical predictions normalised to the nominal values of the FFNS A NLO predictions.

3 PDF constraints from charm CC pseudodata

The impact of charm CC cross section measurements at the LHeC on the PDFs is quantitatively estimated using a profiling technique [37]. This technique is based on minimizing χ^2 between data and theoretical predictions taken into account both experimental and theoretical uncertainties arising from PDF variations. Two NLO PDF sets were chosen for this study: ABMP16 [30] and NNPDF3.1 [33] available via the LHAPDF interface (version 6.1.5) [38]. All PDF sets are provided with uncertainties in the format of eigenvectors.

For this study, pseudodata representing measurements of charm CC production cross sections as a function of Q^2 and x are used. **[TODO: describe how pseudodata were produced]** The study is performed using the xFITTER program (version 2.0.0) [39], an open-source QCD fit framework for PDF determination. The theoretical predictions are calculated at NLO QCD in the FFNS with the number of active flavours $n_f = 3$ and FONLL-B with $n_f = 5$. The running charm mass is set to $m_c(m_c) = 1.27$ GeV and α_s is set to the value used for the corresponding PDF extraction. The renormalisation and factorisation scales are chosen to be $\mu_r = \mu_f = Q^2$.

The χ^2 value is calculated as follows:

$$\chi^2 = \mathbf{R}^T \mathbf{Cov}^{-1} \mathbf{R} + \sum_\beta b_{\beta,\text{th}}^2, \quad \mathbf{R} = \mathbf{D} - \mathbf{T} - \sum_\beta \Gamma_{\beta,\text{th}} b_{\beta,\text{th}}, \quad (5)$$

where $\mathbf{D}$ and $\mathbf{T}$ are the column vectors of the measured and predicted values, respectively, and the correlated theoretical PDF uncertainties are included using the nuisance parameter vector $\boldsymbol{b}_\text{th}$ with their influence on the theory predictions described by $\Gamma_{\beta,\text{th}}$, where index β runs over all PDF eigenvectors. For each nuisance parameter a penalty term is added to the χ^2, representing the prior knowledge of the parameter. No theoretical uncertainties except the PDF uncertainties are considered. The full covariance matrix representing the statistical and systematic uncertainties of the data is used in the fit. The statistical and systematic uncertainties are treated as additive, i.e., they do not change in the fit. The systematic uncertainties are assumed uncorrelated between bins.

To treat the asymmetric PDF uncertainties of the NNPDF3.1 set, the χ^2 function in Eq. 5 is generalised assuming a parabolic dependence of the prediction on the nuisance parameter [39]:

$$\Gamma_{\beta,\text{th}} \to \Gamma_{\beta,\text{th}} + \Omega_{\beta,\text{th}} b_{\beta,\text{th}}, \quad (6)$$

where $\Gamma_{\beta,\text{th}} = 0.5(\Gamma_{\beta,\text{th}}^+ - \Gamma_{\beta,\text{th}}^-)$ and $\Omega_\beta = 0.5(\Gamma_{\beta,\text{th}}^+ + \Gamma_{\beta,\text{th}}^-)$ are determined from the shifts of predictions corresponding to up ($\Gamma_{\beta,\text{th}}^+$) and down ($\Gamma_{\beta,\text{th}}^-$) PDF uncertainty eigenvectors.

The values of the nuisance parameters at the minimum, $b_{\beta,\text{th}}^{\min}$ are interpreted as optimised, or profiled, PDFs, while their uncertainties determined using the tolerance criterion of $\Delta\chi^2 = 1$ correspond to the new PDF uncertainties. The profiling approach assumes that the new data are compatible with theoretical predictions using the existing PDFs, such that no modification of the PDF fitting procedure is needed. Under this assumption, the central values of the measured cross sections are set to the central values of the theoretical predictions.

The original and profiled ABMP16 and NNPDF3.1 PDF uncertainties are shown in Figs. 11–14. The uncertainties of the PDFs are presented at the scales $\mu_f^2 = 100$ GeV^2 and $\mu_f^2 = 100000$ GeV^2. A strong impact of the charm CC pseudodata on the PDFs is observed for both PDF sets. In particular, the uncertainties of the strange PDF are strongly reduced once the pseudodata are included in the fit. Also the gluon PDF uncertainties are decreased. Furthermore, in the case of the NNPDF3.1 set and FONLL scheme, the charm PDF uncertainties are reduced significantly.
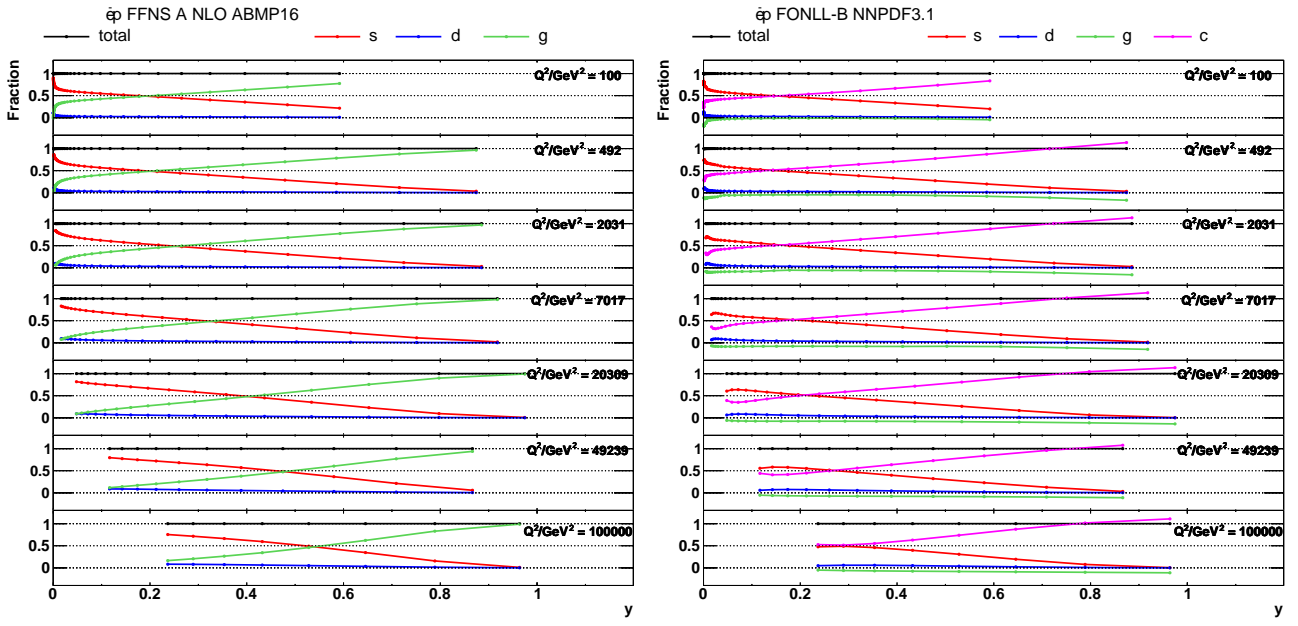
4 Discussion and summary
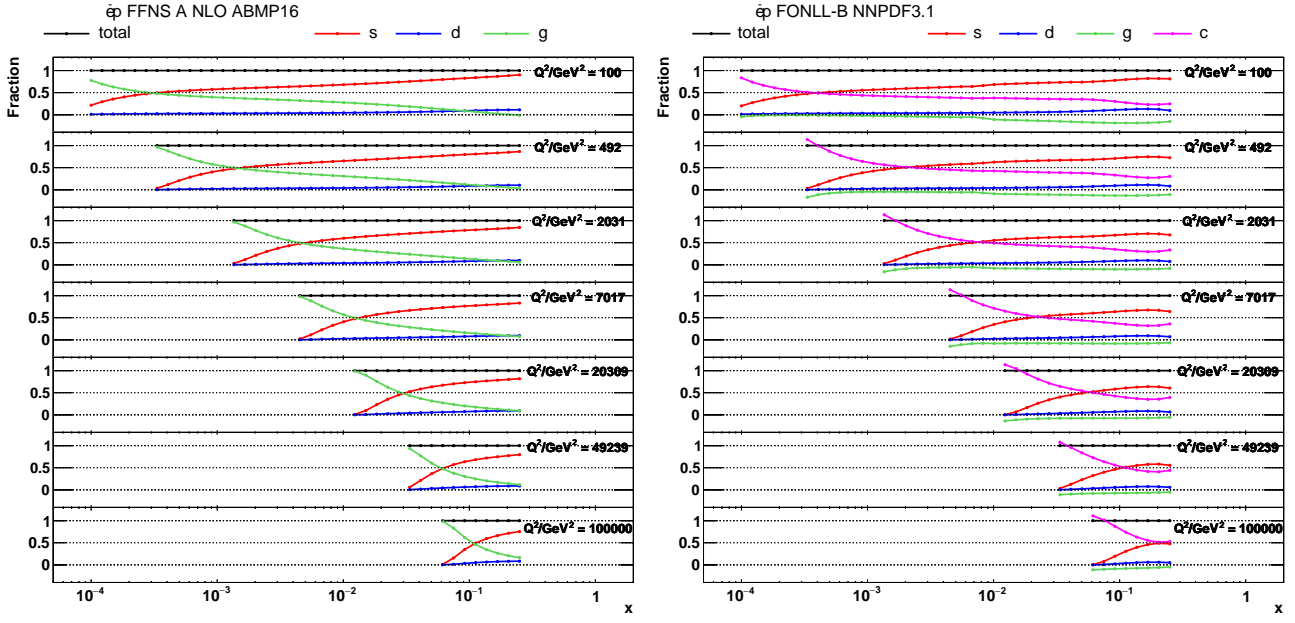
Figure 8 The partonic subprocesses for charm CC production cross sections in the FFNS A (left) and FONLL-B (right) schemes as a function of x_{Bj} for different values of Q^2.
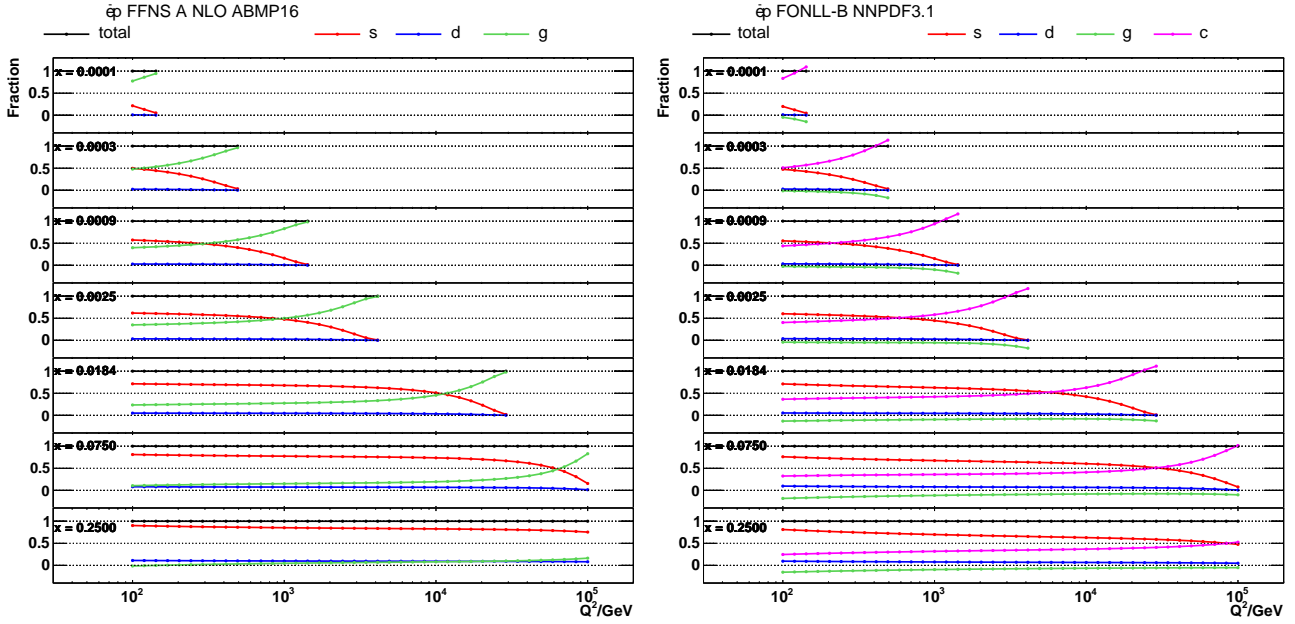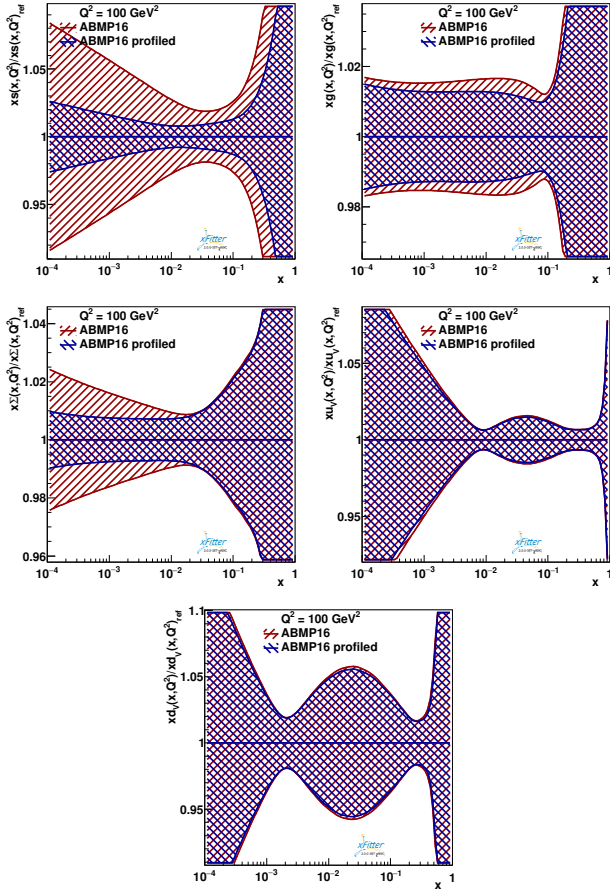

Figure 9 The partonic subprocesses for charm CC production cross sections in the FFNS A (left) and FONLL-B (right) schemes as a function of Q^2 for different values of x_{Bj}.

Figure 10 The partonic subprocesses for charm CC production cross sections in the FFNS A (left) and FONLL-B (right) schemes as a function of y for different values of Q^2.
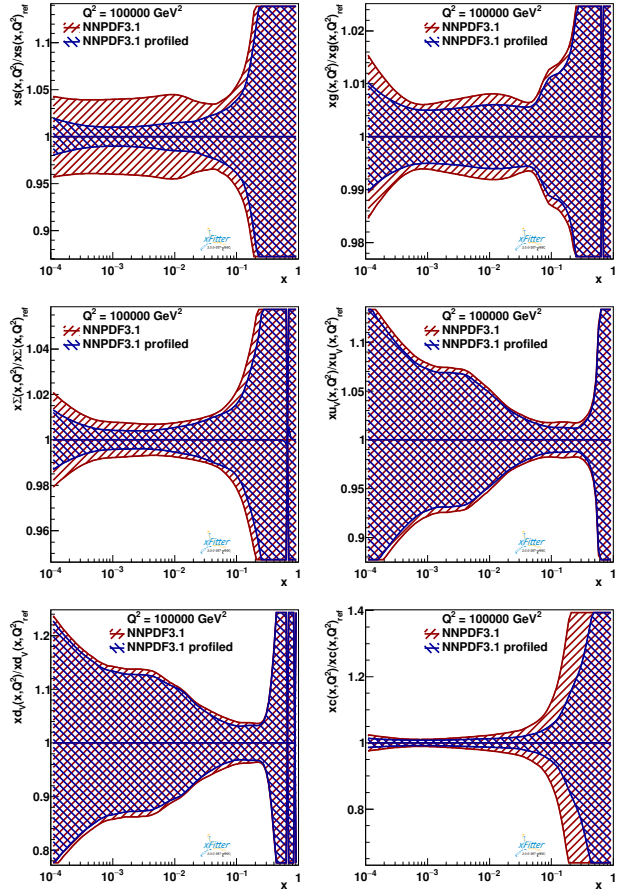
Figure 11 The relative strange (top left), gluon (top right), sea quark (middle left), u valence quark (middle right) and d valence quark (bottom) PDF uncertainties at $\mu_\text{f}^2 = 100$ GeV^2 of the original and profiled ABMP16 PDF set.
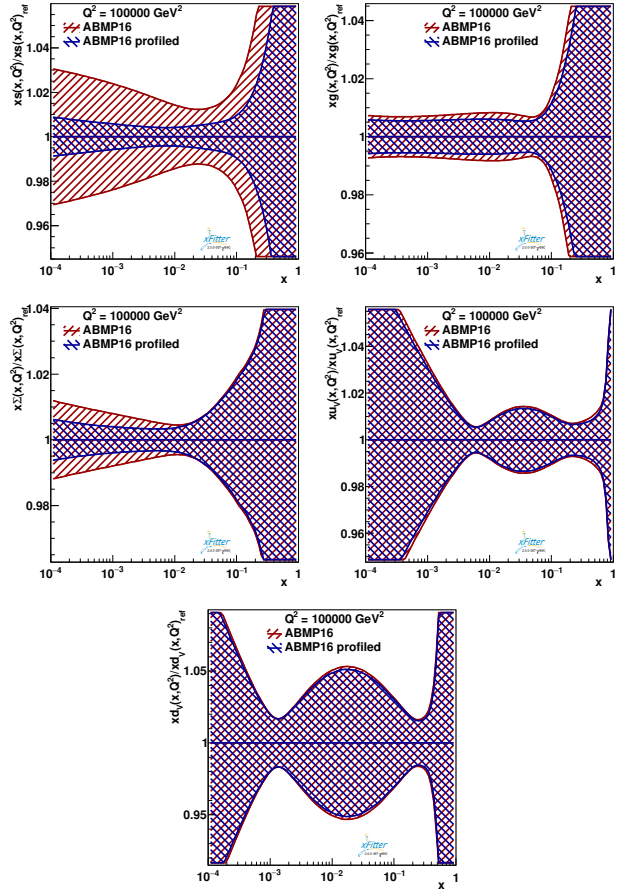
Figure 12 The relative strange (top left), gluon (top right), sea quark (middle left), u valence quark (middle right) and d valence quark (bottom) PDF uncertainties at $\mu_\text{f}^2 = 100000$ GeV^2 of the original and profiled ABMP16 PDF set.
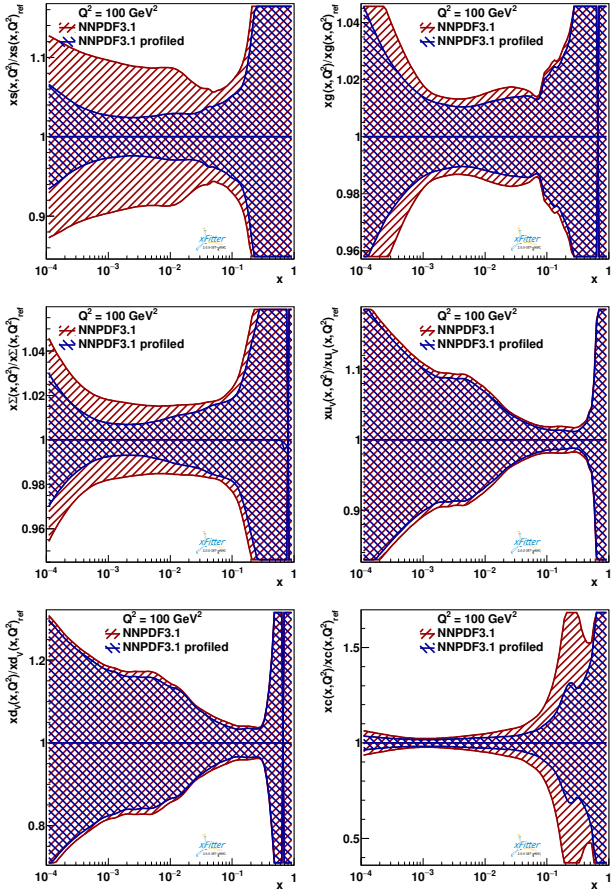
Figure 13 The relative strange (top left), gluon (top right), sea quark (middle left), u valence quark (middle right), d valence quark (bottom left) and charm quark (bottom right) PDF uncertainties at $\mu_\mathrm{f}^2 = 100$ GeV^2 of the original and profiled NNPDF3.1 PDF set.

Figure 14 The relative strange (top left), gluon (top right), sea quark (middle left), u valence quark (middle right), d valence quark (bottom left) and charm quark (bottom right) PDF uncertainties at $\mu_\mathrm{f}^2 = 100000$ GeV^2 of the original and profiled NNPDF3.1 PDF set.
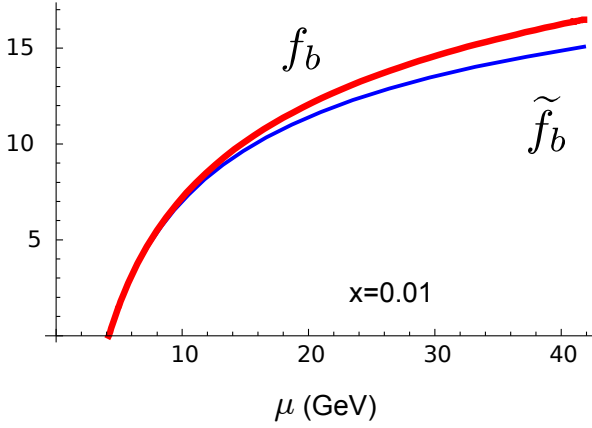
Figure 15 We may switch to charm; I took from our heavy flavor paper. The LO contributions correspond to the heavy quark (Q) initiated f_Q, and the SUB to $\tilde{f}_Q$. The cancellation (LO-SUB) is quite precise. If we were to remove LO or SUB, our TOT result would have anomalous contributions (and correspondingly anomalous μ-dependence) in the region $\mu \sim m_Q$.
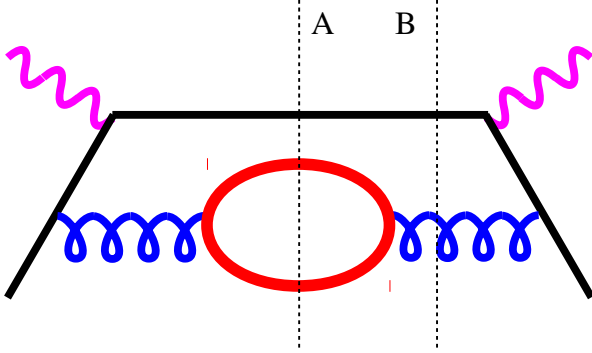
Figure 16 draft in progress: A higher order Feynman graph illustrating the difficulty in defining an "inclusive" F_2^{charm}. If we have a light quark (q) scattering from a vector boson (V), at higher orders we could have a charm–anti-charm loop. If we cut the amplitude with cut "A" we have charm in the final state and this must be included in F_2^{charm}. If we cut the amplitude with cut "B" there is no charm in the final state, but this process is required to satisfy IR divergences as governed by the Kinoshita-Lee-Nauenberg (KLN) theorem. Also note, since this diagram contributes to the beta function, this highlights the difficulty of using an α_S and hard scattering $\hat{\sigma}$ with differing N_{eff}.

Appendix A: Defining F_2^{charm} Beyond Lead Order

The charged current DIS charm production process involves some interesting issues. Because two quark masses are involved $\{m_s, m_c\}$, we can separately examine the mass singularities of the t-channel and u-channel separately; this separation is particularly useful to understand how the FFNS and VFNS divide up the contributions to the total structure function. Additionally, the DIS charm production allows us to identify the deficiencies we encounter due to the fact that a truly "inclusive" F_2^{charm} is not a theoretically well-defined observable.

X

[FRED: THIS INTRO IS STILL ROUGH] Suppose we attempt to compute the "inclusive" F_2^{charm} for Charged Current (CC) charm production at NLO in the VFNS. The obvious LO diagram is ($sW^+ \to c$). What is not so obvious is we also will need ($\bar{c}W^+ \to \bar{s}$). This is because the $\bar{c}$ comes from a gluon splitting to $c\bar{c}$, and the c goes down the beam pipe along with the hadron remnants. All three u-channel terms displayed in Fig. *** are required for the result to be both i) insensitivity to the μ-scale, and ii) be free of mass singularities at large Q^2 scales; but this requires measuring charm quarks in an experimentally unaccessible region—the hadron remnants. This is why a truly "inclusive" F_2^{charm} is ill-defined; it is experimentally unobservable.[4]

What is actually measured experimentally is a differential charm production process which must include a resolution scale (or regulator) to make a cut on charm quarks in the beam fragments; this "non-inclusive" F_2^{charm} (or "exclusive") measurement can be well defined.

For this discussion we will focus on the NLO gluon initiated graphs; there are a parallel set of NLO quark initiated processes, but the principles are fully illustrated by the gluon processes.

Additionally, we note that an "inclusive" F_2^{charm} in the FFNS is also ill-defined; at higher orders we have $g \to c\bar{c}$ processes which make it impossible to separate out a "charm only" contribution from the total F_2.[5]
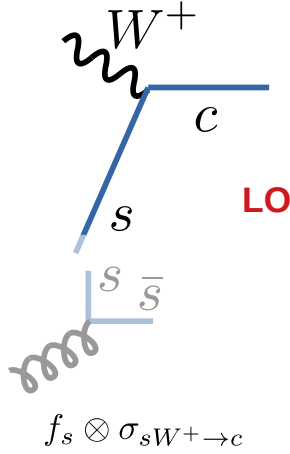
Appendix A.1: t-channel at NLO

The t-channel contributions at NLO are straightforward. We start with a leading-order (LO) $sW^+ \to c$ process. We then add the next-to-leading-order (NLO) $gW^+ \to c\bar{s}$ diagram; this exchanges an s quark in the t-channel, and thus will have a $\ln(m_s^2/Q^2)$ divergence for large Q. This is resolved by the subtraction (SUB) term $f_g \otimes \mathscr{P}_{g \to s} \otimes \sigma_{sW^+ \to c}$ where the $\mathscr{P}_{g \to s}$ represents a perturbative splitting of $g \to s$; the SUB term is proportional to $\mathscr{P}_{g \to s} \sim \frac{\alpha_S}{2\pi} P_{g \to s}^{(1)} \ln(m_s^2/Q^2)$, and will cancel the double counting between the LO and NLO graphs in the limit where the exchanged s quark becomes collinear.[6] The logarithmic divergence (mass singularity) will cancel between the NLO and SUB terms as $Q^2 \to \infty$, resulting in a finite result for the NLO t-channel contribution.
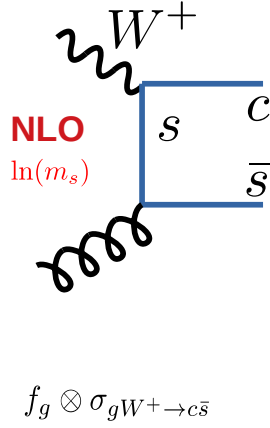
---

[4] The proof of factorization for heavy quarks by Collins cite**** addressed a fully inclusive F_2; it specifically avoided the ill-defined F_2^{charm}.

[5] See for example. Ref. Smith and van Neerven cite*** At $\mathcal{O}(\alpha_S^3)$ we can have internal $g \to c\bar{c}$ processes which make a F_2^{charm} definition ambiguous. This issues is particularly problematic in beta-function which sums over internal quark loops and determines the running of α_S.
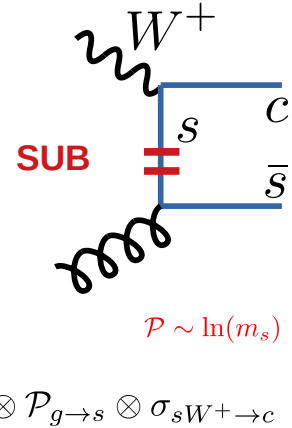
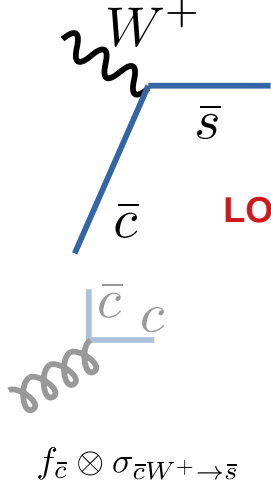[6] Here we use $\mathscr{P}_{g \to s}$ to represent the perturbative splitting contribution which at NLO is given by $\frac{\alpha_S}{2\pi} P_{g \to s}^{(1)} \ln(m_s^2/Q^2)$, where $P_{g \to s}^{(1)}$ is the usual DGLAP splitting kernel.

t-channel

gluon initiated

gluon initiated

$$f_s \otimes \sigma_{sW^+ \to c}$$

$$f_g \otimes \sigma_{gW^+ \to c\bar{s}}$$

$$f_g \otimes \mathcal{P}_{g \to s} \otimes \sigma_{sW^+ \to c}$$

Figure 17 Gluon NLO t-channel processes

u-channel

gluon initiated

gluon initiated

$$f_{\bar{c}} \otimes \sigma_{\bar{c}W^+ \to \bar{s}}$$

$$f_g \otimes \sigma_{gW^+ \to \bar{s}c}$$

$$f_g \otimes \mathcal{P}_{g \to \bar{c}} \otimes \sigma_{\bar{c}W^+ \to \bar{s}}$$

Figure 18 Gluon NLO u-channel processes
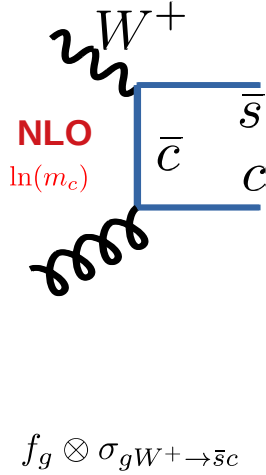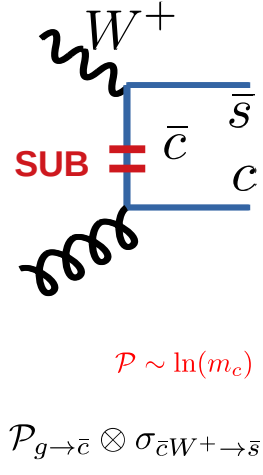
Appendix A.2: u-channel at NLO

The u-channel at NLO is more subtle. We definitely need the NLO $gW^+ \to c\bar{s}$ diagram with a $\bar{c}$ quark exchanged in the u-channel, and thus will have a $\ln(m_c^2/Q^2)$ divergence for large Q. This is resolved by the subtraction term $f_g \otimes \mathcal{P}_{g \to \bar{c}} \otimes \sigma_{\bar{c}W^+ \to \bar{s}}$ where the $\mathcal{P}_{g \to \bar{c}}$ represents a perturbative splitting of $g \to \bar{c}$ and will cancel the double counting between the LO and NLO graphs in the limit where the exchanged $\bar{c}$ quark becomes collinear. Here, the SUB term is proportional to $\mathcal{P}_{g \to \bar{c}} \sim \frac{\alpha_S}{2\pi} P_{g \to \bar{c}}^{(1)} \ln(m_c^2/Q^2)$. The logarithmic divergence will cancel between the NLO and SUB terms as $Q^2 \to \infty$, resulting in a finite result for the NLO u-channel contribution.

Appendix A.3: Why do we need the LO ($\bar{c}W^+ \to \bar{s}$)?

What is not so obvious is that we need the LO u-channel process $\bar{c}W^+ \to \bar{s}$.

Recall that it is essential we include the subtraction SUB term $f_g \otimes \mathcal{P}_{g \to \bar{c}} \otimes \sigma_{\bar{c}W^+ \to \bar{s}}$ so that we get a finite answer at large energies $Q^2 \to \infty$.

At energy scales $Q \sim m_c$, the LO and SUB terms remove the double counting between the LO and NLO processes. This is most apparent when you plot the individual terms versus the Q scale (or more properly, it is the μ scale). [See Figure] In the region of $Q \sim m_c$, the charm PDF f_c (and hence, the LO contribution) rises very quickly as it is driven by the very large gluon, and coupled with a large $\alpha_S(m_c)$. The SUB subtraction also rises quickly as this is driven by the logarithmic term $\ln(m_c^2/Q^2)$. The difference LO-SUB is the physical contribution to the total (TOT=LO+NLO-

SUB), and it is this combination which is smooth across the "turn on" of the charm PDF. We now see that if we neglect the LO ($\bar{c}W^+ \to \bar{s}$) we loose the cancellation between LO and SUB in the $Q \sim m_c$ and our structure function (or cross section) would have an anomalous shift at the location where we arbitrarily turn on the charm PDF.

So to recap, the combination of the LO and SUB terms ensure a minimal μ-variation at low μ scales, and the combination of SUB and NLO ensure the mass singularities are canceled at high μ scales.

Appendix A.4: FFNS: u-channel for $N_F = 3$

Let us clarify the case where we work in a FFNS with 3 flavors $\{u, d, s\}$ but no charm PDF. In this case there is no LO ($\bar{c}W^+ \to \bar{s}$) process as $f_c = 0$, and there is no u-channel subtraction $f_g \otimes \mathscr{P}_{g \to \bar{c}} \otimes \sigma_{\bar{c}W^+ \to \bar{s}}$. This is all perfectly consistent. However, the NLO u-channel process ($gW^+ \to c\bar{s}$) will have a potentially divergent $\ln(m_c^2/Q^2)$ contribution from the exchanged charm quark; this is fine so long as we don't go to large Q. If we do want large Q, then we will need to resum the $\ln(m_c^2/Q^2)$ logs using the charm PDF.

We expect this FFNS to diverge from the VFNS result by contributions proportional to $\sim \frac{\alpha_S}{2\pi} \ln(m_c^2/Q^2)$.

Appendix A.5: The bottom line:

A truly "inclusive" F_2^{charm} is ill-defined. Instead, we necessarily must an "experimentally" defined F_2^{charm} where we specify conditions so that the final state charm is isolated from the hadron remnants.

We can talk about a fully inclusive F_2 where we include all flavors; this was the subject of Collins' proof.

If we compute a "pseudo-inclusive" F_2^{charm} in the Variable Flavor Number Scheme, we do need to include the LO ($\bar{c}W^+ \to \bar{s}$) and the associated SUB ($gW^+ \to c\bar{s}$).

We can compute in the Fixed Flavor Number Scheme, but in the large energy limit, we encounter $\ln(m_c^2/Q^2)$ divergences. In practice, our Q scales are not large enough to generate infinities, but they are large enough where we see the resummed logs included in the VFNS charm PDF become important. Regardless, the FFNS is also unable to define a truly "inclusive" F_2^{charm}.

References

1. H. Abdolmaleki, et al., Eur. Phys. J. **C78**(8), 621 (2018). DOI 10.1140/epjc/s10052-018-6090-8

2. H. Abramowicz, et al., Eur. Phys. J. **C75**(12), 580 (2015). DOI 10.1140/epjc/s10052-015-3710-4

3. J. Gao, L. Harland-Lang, J. Rojo, arXiv:1709.04922 (2017)

4. O. Behnke, A. Geiser, M. Lisovyi, Prog. Part. Nucl. Phys. **84**, 1 (2015). DOI 10.1016/j.ppnp.2015.06.002

5. O. Zenaiev, Eur. Phys. J. **C77**(3), 151 (2017). DOI 10.3204/PUBDB-2017-01474,10.1140/epjc/s10052-017-4620-4

6. H. Abdolmaleki, A. Khorramian, A. Aleedaneshvar, Nucl. Part. Phys. Proc. **282-284**, 27 (2017). DOI 10.1016/j.nuclphysbps.2016.12.006

7. E. Laenen, S. Riemersma, J. Smith, W.L. van Neerven, Nucl. Phys. **B392**, 162 (1993). DOI 10.1016/0550-3213(93)90201-Y

8. E. Laenen, S. Riemersma, J. Smith, W.L. van Neerven, Nucl. Phys. **B392**, 229 (1993). DOI 10.1016/0550-3213(93)90202-Z

9. T. Gottschalk, Phys. Rev. **D23**, 56 (1981). DOI 10.1103/PhysRevD.23.56

10. M. Gluck, S. Kretzer, E. Reya, Phys. Lett. **B398**, 381 (1997). DOI 10.1016/S0370-2693(97)90016-2, 10.1016/S0370-2693(97)00232-3. [Erratum: Phys. Lett.B405,392(1997)]

11. J. Blumlein, A. Hasselhuhn, P. Kovacikova, S. Moch, Phys. Lett. **B700**, 294 (2011). DOI 10.1016/j.physletb.2011.05.007

12. S. Alekhin, J. Blumlein, L. Caminadac, K. Lipka, K. Lohwasser, S. Moch, R. Petti, R. Placakyte, Phys. Rev. **D91**(9), 094002 (2015). DOI 10.1103/PhysRevD.91.094002

13. E.L. Berger, J. Gao, C.S. Li, Z.L. Liu, H.X. Zhu, Phys. Rev. Lett. **116**(21), 212002 (2016). DOI 10.1103/PhysRevLett.116.212002

14. A. Behring, J. BlÃŒmlein, A. De Freitas, A. Hasselhuhn, A. von Manteuffel, C. Schneider, Phys. Rev. **D92**(11), 114005 (2015). DOI 10.1103/PhysRevD.92.114005

15. V.M. Abazov, et al., Phys. Lett. **B743**, 6 (2015). DOI 10.1016/j.physletb.2015.02.012

16. H.L. Lai, P.M. Nadolsky, J. Pumplin, D. Stump, W.K. Tung, C.P. Yuan, JHEP **04**, 089 (2007). DOI 10.1088/1126-6708/2007/04/089

17. W.G. Seligman, et al., Phys. Rev. Lett. **79**, 1213 (1997). DOI 10.1103/PhysRevLett.79.1213

18. M. Tzanov, et al., Phys. Rev. **D74**, 012008 (2006). DOI 10.1103/PhysRevD.74.012008

19. G. Onengut, et al., Phys. Lett. **B632**, 65 (2006). DOI 10.1016/j.physletb.2005.10.062

20. J.P. Berge, et al., Z. Phys. **C49**, 187 (1991). DOI 10.1007/BF01555493

21. O. Samoylov, et al., Nucl. Phys. **B876**, 339 (2013). DOI 10.1016/j.nuclphysb.2013.08.021

22. A. Airapetian, et al., Phys. Lett. **B666**, 446 (2008). DOI 10.1016/j.physletb.2008.07.090

23. T. Aaltonen, et al., Phys. Rev. Lett. **100**, 091803 (2008). DOI 10.1103/PhysRevLett.100.091803
24. V.M. Abazov, et al., Phys. Lett. **B666**, 23 (2008). DOI 10.1016/j.physletb.2008.06.067
25. S. Kretzer, H.L. Lai, F.I. Olness, W.K. Tung, Phys. Rev. **D69**, 114005 (2004). DOI 10.1103/PhysRevD.69.114005
26. A.D. Martin, R.G. Roberts, W.J. Stirling, R.S. Thorne, Phys. Lett. **B604**, 61 (2004). DOI 10.1016/j.physletb.2004.10.040
27. M. Aaboud, et al., Eur. Phys. J. **C77**(6), 367 (2017). DOI 10.1140/epjc/s10052-017-4911-9
28. A.D. Martin, W.J. Stirling, R.S. Thorne, G. Watt, Eur. Phys. J. **C63**, 189 (2009). DOI 10.1140/epjc/s10052-009-1072-5
29. S. Alekhin, J. Blümlein, S. Moch, R. Placakyte, Phys. Rev. **D96**(1), 014011 (2017). DOI 10.1103/PhysRevD.96.014011
30. S. Alekhin, J. Blümlein, S. Moch, Eur. Phys. J. **C78**(6), 477 (2018). DOI 10.1140/epjc/s10052-018-5947-1
31. S. alekhin, "openqcdrad". URL http://www-zeuthen.desy.de/~alekhin/OPENQCDRAD/
32. V. Bertone, S. Carrazza, J. Rojo, Comput. Phys. Commun. **185**, 1647 (2014). DOI 10.1016/j.cpc.2014.03.007
33. R.D. Ball, et al., Eur. Phys. J. **C77**(10), 663 (2017). DOI 10.1140/epjc/s10052-017-5199-5
34. M. Tanabashi, et al., Phys. Rev. **D98**(3), 030001 (2018). DOI 10.1103/PhysRevD.98.030001
35. V. Bertone, et al., Eur. Phys. J. **C77**(12), 837 (2017). DOI 10.1140/epjc/s10052-017-5407-3
36. A. Kusina, F.I. Olness, I. Schienbein, T. Jezo, K. Kovarik, T. Stavreva, J.Y. Yu, Phys. Rev. **D88**(7), 074032 (2013). DOI 10.1103/PhysRevD.88.074032
37. H. Paukkunen, P. Zurita, (2014)
38. A. Buckley, J. Ferrando, S. Lloyd, K. Nordström, B. Page, M. Rüfenacht, M. Schönherr, G. Watt, Eur. Phys. J. C **75**, 132 (2015). DOI 10.1140/epjc/s10052-015-3318-8
39. S. Alekhin, et al., Eur. Phys. J. **C75**(7), 304 (2015). DOI 10.1140/epjc/s10052-015-3480-z